

Cluster Difference Imaging Photometric Survey. III. An Open Cluster Spanning 500 Parsecs

L. G. BOUMA,¹ J. L. CURTIS,^{2,3} J. D. HARTMAN,¹ J. N. WINN,¹ AND G. Á. BAKOS¹

¹Department of Astrophysical Sciences, Princeton University, 4 Ivy Lane, Princeton, NJ 08540, USA

²Department of Astronomy, Columbia University, 550 West 120th Street, New York, NY 10027, USA

³Department of Astrophysics, American Museum of Natural History, Central Park West, New York, NY 10024, USA

(Received —; Revised —; Accepted —)

Submitted to AAS journals.

ABSTRACT

Recent analyses of the Gaia data have reported the existence of diffuse stellar populations surrounding nearby open clusters. It is important to verify that these “halos”, “tails”, and “strings” are of similar ages and compositions as stars in the denser part of the cluster. We present an analysis of NGC 2516 (≈ 150 Myr), which has a classical tidal radius of 10 pc and an apparent halo of stars spanning 500 pc. Combining photometry from Gaia, rotation periods from TESS, and lithium measurements from Gaia-ESO and GALAH, we find that the halo of NGC 2516 is real and coeval with the core. Two thirds of kinematically selected halo members out to 250 pc from the cluster center have rotation periods consistent with a gyrochronological age of 150 Myr. A comparison sample of field stars shows no such trend. In addition, the lithium abundances of stars in the halo are elevated relative to the field, and are correlated with the stellar rotation rate in a manner consistent with previous observations of the Pleiades and Psc Eri. Broadly speaking, this work advances the paradigm in which the halos of many open clusters are more populous than their cores. We highlight the implications for spectroscopic survey targeting, open cluster dispersal, and planet searches around young stars.

Keywords: stellar ages (1581), stellar associations (1582), open clusters (1160), stellar dynamics (1596), stellar rotation (1629)

1. INTRODUCTION

Star clusters form when dense filaments in hierarchically structured molecular clouds collide and collapse (Shu et al. 1987). Over the first 10 Myr, feedback effects including protostellar outflows, photoionization, radiation pressure, and supernova shocks disperse the gas out of the cloud (Krumholz et al. 2019). Since only $\sim 1\%$ of the cloud mass is converted into stars, gas dispersal enables the majority ($\sim 90\%$) of stars in the cluster to escape the cluster’s gravitational well (Lada & Lada 2003).

From 10 to 1000 Myr, the cluster remnants that survive gas dispersal suffer an onslaught that almost always leads to dissolution. Inside the cluster supernovae, AGB winds, and close stellar encounters lead to additional mass loss (Lamers et al. 2010). Extrinsic to the cluster, collisions with giant molecular clouds (Spitzer 1958), and perturbations from the galactic tide in both the radial and vertical dimensions further promote stellar escape (e.g., Fukushige & Heggie 2000; Bergond et al. 2001).

Corresponding author: L. G. Bouma
luke@astro.princeton.edu

Finding the stars that have dispersed from their natal clusters into the galactic field is a pressing topic for a few reasons. One is to understand the spatial extent and duration of star formation events (e.g., Wright & Mamajek 2018). Another is to understand the Sun’s birth environment (Adams 2010). Did the Sun form in an open cluster, and if so, what type? Is there any hope at identifying the stars that formed near the Sun? Open clusters and their dispersed remnants also provide a test case for “chemical tagging” (e.g., Freeman & Bland-Hawthorn 2002; Hogg et al. 2016; Ness et al. 2018). The converse holds too: one can use chemical tagging to test the viability of kinematic clustering methods.

A separate project that benefits from the new discoveries of dispersed stellar populations is that of finding young transiting exoplanets. Young transiting planets are hard to find because young stars are rare, and mostly reside in the crowded galactic plane (see e.g., Kharchenko et al. 2013; Piskunov et al. 2018). If the dispersed halos of nearby star clusters could be reliably identified, this could expand the census of nearby young stars by up to a factor of 10, based on the expected fraction of stars thought to be lost during gas dispersal.

The detection of dispersed stellar associations, although possible before Gaia, has now reached a breakthrough pace

(e.g., de Zeeuw et al. 1999; Bergond et al. 2001; Zuckerman & Song 2004; Oh et al. 2017; Cantat-Gaudin et al. 2018; Gagné et al. 2018; Gagné & Faherty 2018; Kounkel et al. 2018; Zari et al. 2018; Kounkel & Covey 2019; Fürnkranz et al. 2019). The populations found by these studies can be summarized as follows. On one end are coeval groups with no discernable cores (e.g., Psc Eri and μ Tau, Meingast et al. 2019; Curtis et al. 2019; Gagné et al. 2020). On the other are hierarchically structured associations with many over and under-densities (e.g. the Sco-Cen and Vela associations Pecaut & Mamajek 2016; Cantat-Gaudin et al. 2019). Here, we focus on an intermediate regime: low-density halos associated with a single overdensity, typically an open cluster that was known before Gaia (see Kounkel & Covey 2019; Kounkel et al. 2020; Meingast et al. 2021). In some cases, these halos could correspond to tidal tails, as have been reported in the Hyades (Meingast & Alves 2019; Röser et al. 2019), the Ursa Major moving group (Gagné et al. 2020), and in Coma Berenices (Tang et al. 2019).

One point of difficulty however is that different clustering methods yield differing levels of sensitivity and precision (Hunt & Refert 2020). Using say a Gaussian Mixture Model tautologically yields open clusters that are elliptical (e.g., Wallace 2018). Some unsupervised methods yield dispersed and asymmetric structures with number densities down to 100 times less than the field around the same regions (see e.g., Kounkel & Covey 2019 and Meingast et al. 2021). Differences between different clustering methods raise the issue of how contaminated the resulting samples are, and in some cases whether the reported structures are truly coeval stellar populations at all.

We have recently been making TESS light curves of stars reported to be members of coeval populations (CDIPS, Bouma et al. 2019). Our analysis of TESS Sectors 1-13 yielded light curves of 483,407 candidate cluster members in the Southern Ecliptic hemisphere, which are available on MAST¹.

As part of this broader project, we focus here on a modest question: in just a single southern open cluster, is the cluster halo truly coeval with the core? We chose NGC 2516 for this analysis since it is young (100–200 Myr) and sufficiently nearby ($d \approx 400$ pc) to facilitate photometric rotation measurements using TESS. Its halo was recently reported by Kounkel & Covey (2019) to span $\approx 20 \times 10 \times 350$ pc. We want to know: is this halo real? To what extent can we use Gaia alone to reliably identify age-dated needles in the haystack of field stars? What are the implications, observationally and theoretically, if we can identify the dispersed halos of open clusters?

A brief note on terminology. Low-density stellar associations connected to a dense population (a “core”) have been described as being in “halos”, “strings”, “coronae”, “snakes”, “outskirts”, and “tidal tails” (e.g., Davenport & Sandquist 2010; Kounkel & Covey 2019; Röser et al. 2019; Tian 2020;

Meingast et al. 2021). The latter term implies a particular model for the formation of the dispersed group. “Halo” is concise and model agnostic, but suffers from the suggestion of spherical symmetry. The halo of NGC 2516 is most accurately described as consisting of a leading and trailing tail. However, the goal of this study is to clarify whether the stars in these tails are the same age as stars in the core, and not to make a ruling on the origin of the overall structure. For this reason, we adopt the model-agnostic “halo”.

Section 2 summarizes the astrometric analyses of the Gaia data that led to our interest in NGC 2516. Section 3 measures the age of the cluster’s halo and core using Gaia photometry (Section 3.1), TESS gyrochronology (Section 3.2), and lithium depletion (Section 3.3). In Section 4 we discuss the implications of our analysis for NGC 2516 specifically and stellar spin-down and open cluster evolution generally. Section 5 gives our conclusions.

2. A DISPERSED HALO AND A CORE?

We selected candidate NGC 2516 members based on those reported in the literature. While some pre-Gaia analyses were available (Jeffries et al. 2001; Kharchenko et al. 2013), the purity and accuracy of the Gaia-derived results are the current state of the art. We therefore adopted what we viewed as the most important clustering samples to compare: those of Cantat-Gaudin et al. (2018), Kounkel & Covey (2019) and Meingast et al. (2021). We refer to these studies in the following as CG18, KC19, and M21 respectively. A useful visualization of these samples is available online². While we considered performing our own clustering analysis on the Gaia data, such an effort would in effect only replicate the work of these investigators. We opt to instead use their studies as a starting point.

The Gaia clustering studies each used different selection functions, which yielded different results. CG18 considered stars brighter than $G = 18$ mag within a few degrees of the center of NGC 2516, and reported 1106 candidate cluster members. KC19 and M21 considered stars up to ≈ 1 mag fainter, and reported 3003 and 1860 members respectively. The unsupervised clustering techniques that each of these studies applied to the second Gaia data release are discussed in Appendix A, as is the overlap between their resulting membership catalogs.

Figure 1 shows the cluster members reported by each study in the space of observed positions, proper motions, and radial velocity when available. In Figure 1, and for the remainder of the study, we describe the CG18 members as the “core” of the cluster, and any non-overlapping KC19 and M21 members as the “halo”. This definition implies that there are 1,106 core members, and 2,2192 halo members. The distinction is tautological, in the sense that CG18 did not extend their search for members out to tens of degrees from the cluster center. Nonetheless, the CG18 membership catalog is

¹ <https://archive.stsci.edu/hlsp/cdips>

² <https://homepage.univie.ac.at/stefan.meingast/coronae.html>, made by Meingast et al. (2021), last accessed 2021/04/05.

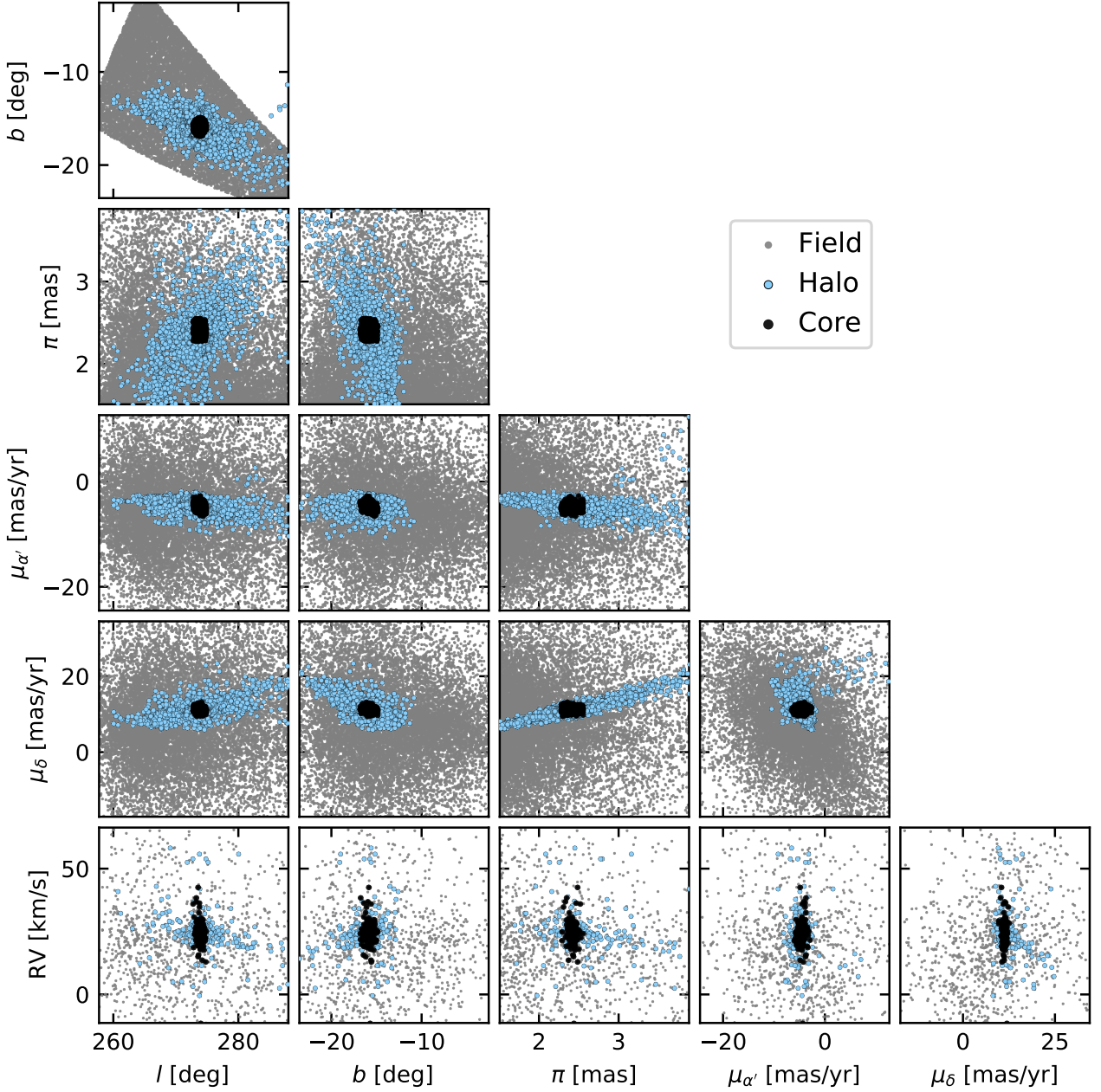


Figure 1. The dense and diffuse components of NGC 2516 across position and velocity space. The core (black) was analyzed by Cantat-Gaudin et al. (2018) using Gaia DR2, and is coincident with the visual overdensity of stars canonically accepted as “the cluster”. The halo (blue) is a concatenation of studies by Kounkel & Covey (2019) and Meingast et al. (2021), which used less restrictive membership assignment algorithms described in Appendix A. The field sample is randomly drawn from a (α, δ, π) cube centered on the cluster. The low volume density of the halo stars makes it difficult to visually distinguish the field and the halo samples.

consistent with that of many earlier investigators (e.g., Jeffries et al. 2001; Kharchenko et al. 2013), and is consistent with the general visual overdensity one sees when viewing NGC 2516 in the sky: it appears to span $\approx 2^\circ$, not $\approx 20^\circ$.

Outside of the core and halo, we also define a set of nearby field stars in the “neighborhood” of NGC 2516. Based on the observed distribution of halo members, we drew these stars randomly from the following intervals of right ascen-

sion, declination, and parallax:

$$\alpha [\text{deg}] \in [108, 132], \quad (1)$$

$$\delta [\text{deg}] \in [-76, -45], \quad (2)$$

$$\pi [\text{mas}] \in [1.5, 4.0]. \quad (3)$$

We imposed a magnitude limit of $G = 19$ mag, and ran the queries using the `astroquery.gaia` module (Ginsburg et al. 2018). We allowed the number of stars in the compar-



Figure 2. Position and orbit of NGC 2516 in the Galaxy. Points denote halo members with $\pi/\sigma_\pi > 20$. In our galactic coordinate system, the Sun is at $\{X, Y, Z\} = \{-8122, 0, +20.8\}$ pc. The gray line traces the past and future cluster orbit. In different projections, the gray line spans different time intervals: the longest time window is visible in the (Z, X) projection. The large blue arrows denote the median cluster velocity after subtracting the local standard of rest: $\{v_X, v_Y, v_Z\} = \{-22.2, -25.3, -4.6\}$ km s $^{-1}$. By comparison, $\vec{v}_{\text{LSR}} = \{12.9, 245.6, 7.78\}$ km s $^{-1}$; in the inertial frame of the Galaxy, NGC 2516 is moving mostly in the \hat{Y} direction. The sizes of the blue arrows are internally proportionate.

ison sample to exceed that in the cluster sample by a factor of ≈ 5 , to ensure broad sampling of stellar masses and evolutionary states. We also required the comparison sample to not overlap with the cluster sample.

The style of visualization given in Figure 1 does not make it clear, in our eyes, why the clustering algorithms have decided to associate certain stars with the halo. Canonically, open clusters are spherical, and span ≈ 10 pc (e.g., Kharchenko et al. 2013). Inverting the parallaxes in Figure 1 shows that members have been reported from line-of-sight distances ranging from ≈ 300 to ≈ 600 pc. Is this structure real? What explains its existence?

An initial step in visualizing the reported structure and kinematics of the candidate cluster members is to consider them in Cartesian coordinates (Figure 2). We computed the physical positions by transforming from (α, δ, π) to galactocentric (X, Y, Z) assuming the astropy v4.0 coordinate standard (Astropy Collaboration et al. 2018). The direction of galactic rotation is $+Y$. The cluster orbit (gray line) was evaluated by taking the median parameters for core members for which CG18 reported membership probabilities exceeding 70%. We then integrated the orbit using `galaxia` and the MWPotential2014 potential (Bovy 2015; Price-Whelan 2017).

The general shape of the cluster itself seems to include a central overdensity and two tails (the halo). One tail is leading the cluster’s orbit, and is angled toward the center of the galaxy when viewed top-down. The other tail is trailing the cluster’s orbit, and is pointed away from the center of the galaxy. The elongation of the cluster in both the (X, Y) and (Z, Y) planes is correlated with the direction of the LSR-corrected median cluster velocity. Possible explanations for this overall morphology are discussed in Section 4.1.

3. AGE-DATING THE HALO OF NGC 2516

3.1. HR Diagram from Gaia

The first check on whether the candidate cluster members share the same age is to analyze the Gaia Hertzsprung-Russell (HR) diagrams. Comparable analyses have previously been performed by CG18, KC19, and M21.

Figure 3 shows the HR diagram in the space of absolute Gaia G magnitude as a function of observed Bp–Rp color. Stars in the core appear consistent with having a fixed age and metallicity, and varying mass. The halo stars show a similar sequence, though with greater scatter. One possible explanation for the additional scatter could be that the halo is more contaminated by field stars. For instance, ≈ 5 red giants in the halo must be field interlopers, because their isochronally implied ages would be inconsistent with that of the cluster.

A second possible explanation for scatter in the halo’s HR diagram could be differential reddening across different sightlines. The reported halo spans 20° on-sky, and varies in position from about $b = -12^\circ$ to $b = -20^\circ$, with the stars closest to the galactic plane also being further from the Sun by up to 300 pc (Figure 1). Some empirical evidence for differential reddening is discussed in Appendix E. Based on the available evidence, we expect that both field star contamination and differential reddening could play a role in the larger scatter of the halo relative to the core. A third possibility that we have not explored is whether the binary fraction could also differ between the different regions of the cluster.

In the right panel of Figure 3, we compare the observed Gaia EDR3 photometry with PARSEC isochrones (Bressan et al. 2012; Chen et al. 2014, 2015; Marigo et al. 2017). We used the web interface³ to interpolate these isochrones at $\log_{10}(t/\text{yr}) = \{8, 8.25, 8.5\}$.

³ <http://stev.oapd.inaf.it/cgi-bin/cmd>, 2021-02-26, CMD3.4, YBC bolometric corrections as in Chen et al. (2019).

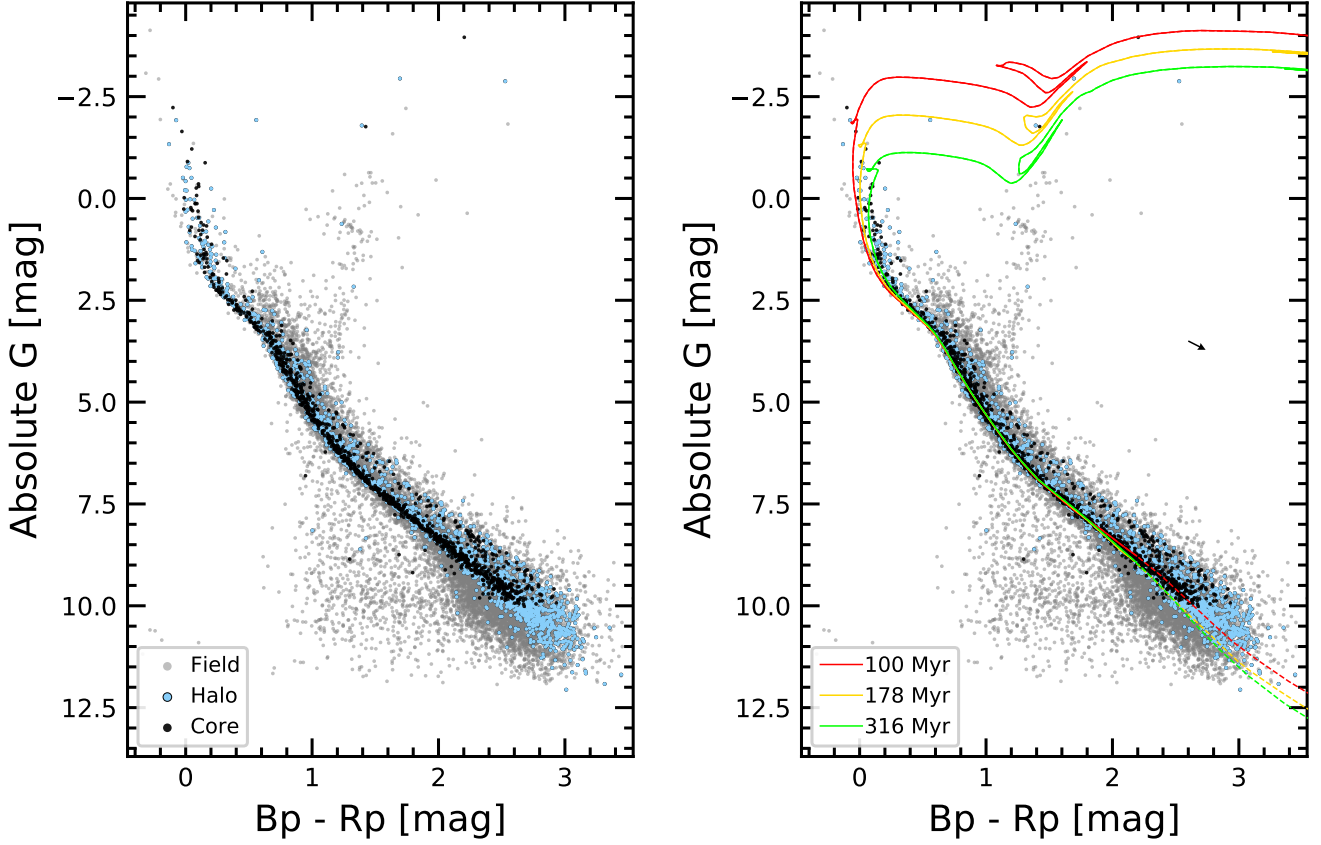


Figure 3. HR diagrams of NGC 2516. *Left:* Photometric data from Gaia EDR3; no reddening correction has been applied. The core (black) shows a main-sequence and turnoff consistent with stars of a fixed age and metallicity. The halo (blue) is similar, though the binary sequence is less defined. The faintest M dwarfs in the core and halo are brighter than field stars (gray) with the same color, consistent with the cluster M dwarfs not having yet reached the main-sequence. *Right:* PARSEC isochrones ($[Fe/H]=+0.06$) are overplotted at intervals of $\log_{10}(t/\text{yr}) = \{8, 8.25, 8.5\}$. The arrow represents the average reddening correction applied to the models. The opacity of the M-dwarf model atmospheres is less well-calibrated for $M_* \lesssim 0.45M_\odot$ ($\approx M2V$; $Bp-Rp \approx 2.2$); these model values are shown with dashed lines.

To determine the reddening correction across NGC 2516, we queried the 2MASS DUST service⁴ and retrieved the extinction parameters at the positions of each NGC 2516 member. The mean and standard deviation of the $E(B-V)$ values for the Schlegel et al. (1998) and Schlafly & Finkbeiner (2011) maps were consistent, so we adopted the average from Schlegel et al. (1998): $E(B-V)_S = 0.206 \pm 0.039$. Bonifacio et al. (2000) found however that the Schlegel et al. (1998) maps overestimate the reddening values when the color excess exceeds about 0.10 mag. Applying the correction proposed by Bonifacio et al. (2000) leads to our adopted $E(B-V) = 0.102 \pm 0.019$. Finally, to convert to Gaia colors we used the calibration of Stassun et al. (2019), namely $E(Bp-Rp) = 1.31E(B-V)$ and $A_G = 2.72E(B-V)$. This yielded $E(Bp-Rp) = 0.134 \pm 0.025$, which is used in the plots. To redden the isochrones, we assumed $R_V = 3.1$, and

applied the O'Donnell (1994) SED-dependent extinction law star-by-star through the PARSEC interface.

For the metallicity, we considered a range of super and sub-solar metallicities to fit as much of the locus from $0.5 < Bp-Rp < 1.5$ as possible, and settled on the slightly super-solar $[M/H] = 0.06$ (Cummings 2011). Sub-solar metallicities led to model predictions too blue along the main sequence by ≈ 0.1 mag. Our adopted metallicity agrees with the spectroscopic metallicity from Cummings (2011, Sec 4.4.4), and with the iron abundance recently determined by the Gaia-ESO team (Baratella et al. 2020), which represented an up-revision from an earlier sub-solar metallicity (Randich et al. 2018). While Bailey et al. (2018) report a slightly sub-solar metallicity for the cluster, we prefer super-solar based on the goodness of fit from the photometry.

Overall, the data and models agree for masses above $\approx 0.45M_\odot$. Below this mass, the data and models diverge at colors redder than $Bp-Rp \approx 2.2$, in the sense that the model isochrones have lower luminosities and bluer colors

⁴ <http://irsa.ipac.caltech.edu/applications/DUST>; query performed using the astrobase.services.dust module (Bhatti et al. 2018).

than the observations.⁵ The MIST isochrones showed a comparable disagreement (Choi et al. 2016). Proposed explanations for the discrepancy between the models and observations have include starspots and incomplete molecular line lists (e.g., Stauffer et al. 2003; Feiden & Chaboyer 2013; Rajpurohit et al. 2013; Mann et al. 2013; Choi et al. 2016). Ultimately, we adopted the PARSEC isochrones because Chen et al. (2014) implemented an empirical temperature-opacity calibration, which leads the PARSEC isochrones to diverge at slightly lower mass than the MIST models. Regardless, for purposes of age-dating the cluster we focus on the main-sequence turn-off (MSTO), since this is where the models have maximal predictive power.

Cummings & Kalirai (2018) presented techniques for mitigating some of the complexities of MSTO age-dating (e.g., sparse turnoffs, stellar rotation, high binarity fractions, and the presence of blue stragglers). Combining a *UBV* color-color analysis with Gaia DR2 cluster memberships, they found MSTO ages for NGC 2516 ranging from 165 to 195 Myr, depending on the choice of model isochrone (Y², PARSEC, MIST, or SYCLIST).

Our goal is to determine whether the ages of the core and halo are consistent. The left panel of Figure 3 suggests that isochronally, they are: stars past the turnoff in both the halo and core are on a consistent locus. The right panel of Figure 3 demonstrates the precision with which the claim can be made. The MSTO stars are consistent with the 178 and 316 Myr models, but are bluer than the 100 Myr model. The red-giant-branch (RGB) stars are consistent only with the 178 Myr ($\log_{10} t/\text{yr} = 8.25$) model. Based on the assumption that the width of the MSTO can be attributed to binary stars, we are most interested in the blue edge (blue stragglers are, however, a concern). The blue edge appears most compatible with the 178 Myr model. These results are consistent with the MSTO age range of 165 to 195 Myr found by Cummings & Kalirai (2018), and we refer to their work for the more precise model-dependent comparison. Based on Table 3 of Cummings & Kalirai (2018), we therefore adopt a PARSEC-based isochrone age for NGC 2516 of 165 ± 35 Myr, where our quoted uncertainty is a quadrature sum of the statistical and systematic components from Cummings & Kalirai (2018).

3.2. Rotation from TESS

3.2.1. Methodology

We began our rotation analysis by considering all 3,298 candidate members of NGC 2516. For each source, we retrieved all available CDIPS light curves, on a per-sector basis. This yielded 2,205 stars with at least one sector from a CDIPS light curve. Each of these stars is brighter than the CDIPS magnitude limit of $R_p = 16$ mag. 2,270 of the stars from the NGC 2516 source list had $R_p < 16$. The difference (65 stars) is due to 35 stars from Meingast et al. (2021) which

⁵ The 100 Myr isochrone does overlap well with the lower main sequence, but it fails to fit the upper main sequence and red giants.

were not available at the time of the CDIPS reductions, and 30 stars falling on the TESS chip gaps. The $R_p = 16$ mag cutoff imposed during the CDIPS processing corresponds roughly to $(B_p - R_p)_0$ of 2.2, or a spectral type of \approx M2V, at the distance of NGC 2516.

We removed systematic trends shared between all light curves on each CCD in each sector individually, and stitched together the resulting light curves before searching for rotation-induced periodicity. Details regarding our detrending approach are presented in Appendix B. After applying the initial ensemble decorrelation to remove systematic trends, we proceeded with a few cleaning steps: we masked 0.7 days at the beginning and end of each spacecraft orbit, and ran a sliding standard-deviation rejection window over the light curve, which removed any outlying points within $\pm 3 \times \text{MAD}$ of the median in each window.

We then measured the rotation period from the resulting light curve using the periodogram implementations in astrobase, namely the traditional Lomb-Scargle, and the Stellingwerf phase-dispersion minimization algorithm (Lomb 1976; Stellingwerf 1978; Scargle 1982; Stellingwerf 2011; Bhatti et al. 2018). We used the CDIPS aperture radius that, based on theoretical expectations, was expected to give the optimal balance between light from the target star and background-light (Sullivan et al. 2015). This typically resulted in an aperture radius of either 1 or 1.5 pixels. We recorded the top five periodogram peaks from each method, and their corresponding powers. Finally, as a check on crowding, we recorded the number of stars within the aperture with equal or greater brightness than the target star, and with brightness within 1.25 and 2.5 TESS magnitudes of the target star.

To clean the resulting rotation period measurements, we designed a set of automated cleaning criteria, which yielded sets we denote \mathcal{A} and \mathcal{B} . For both sets, we considered light curves for which the peak Lomb-Scargle periodogram period was below 15 days, the normalized Lomb-Scargle power exceeded 0.08, and for which no equal-brightness or greater companions were within the aperture. Beyond requiring that the target star be the brightest star in the aperture, we also required that at most one companion with brightness exceeding one tenth of the target star’s brightness be present in the aperture according to the Gaia DR2 source catalog. For set \mathcal{A} , this yielded 987 light curves, out of 1,641 stars for which rotation periods might plausibly have been detected. For set \mathcal{B} , we additionally required that the Lomb-Scargle and Stellingwerf phase-dispersion methods yielded identical periods to within 10%. This yielded 507 light curves.

3.2.2. Rotation-Color Diagrams

The top row of Figure 4 shows the resulting rotation periods, with set \mathcal{A} shown the left and \mathcal{B} on the right. While set \mathcal{A} is more complete than set \mathcal{B} , this completeness comes at the expense of greater contamination. For instance, stars above the slow sequence (perhaps field contaminants) mostly disappear in set \mathcal{B} . The “void” or “gap” underneath the slow sequence is also more pronounced in set \mathcal{B} . To facilitate a

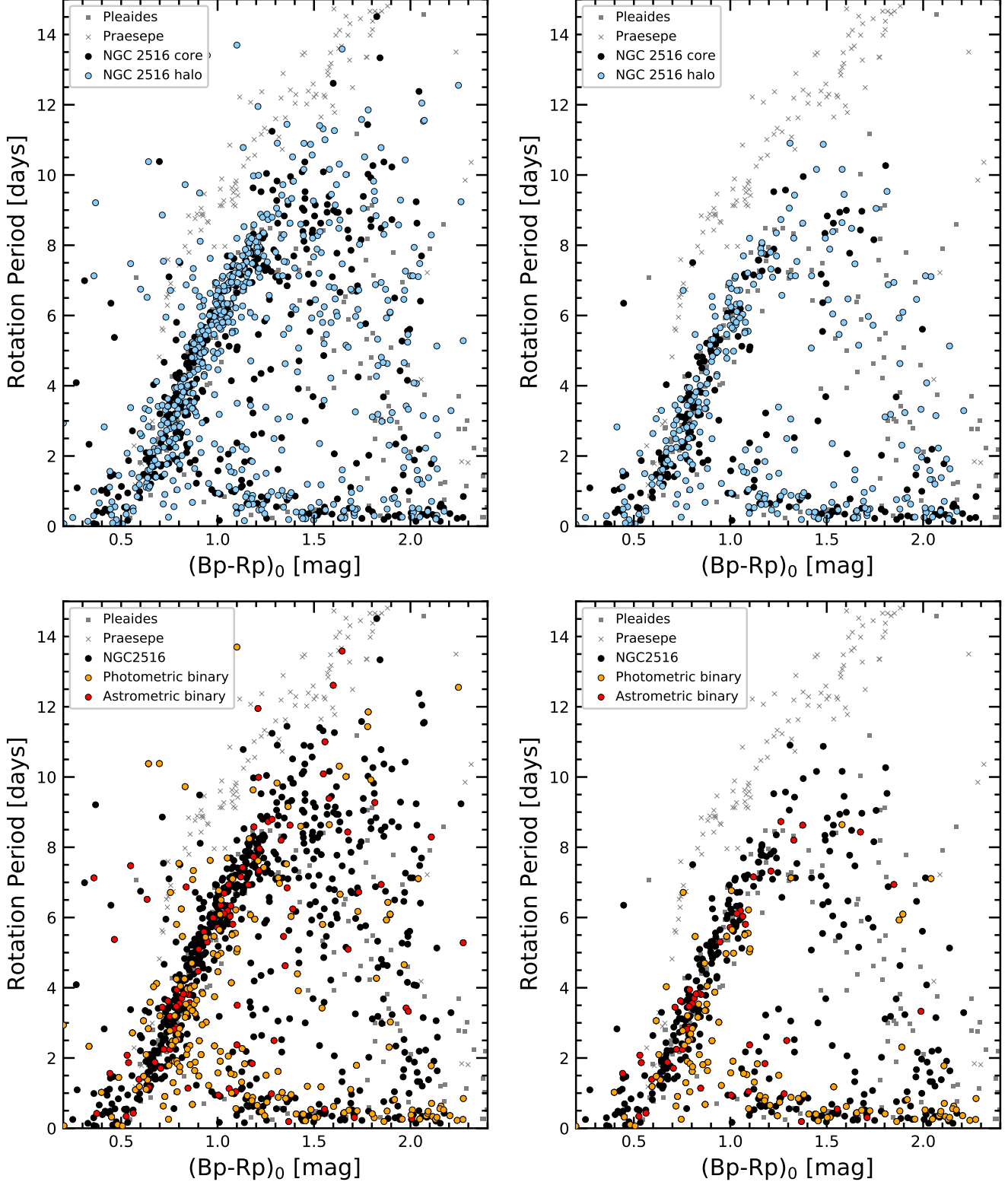


Figure 4. TESS rotations periods and dereddened Gaia colors for NGC 2516. *Top row:* NGC 2516 split into its core and halo. Sets \mathcal{A} (left) and \mathcal{B} (right) undergo successive stages of automated cleaning, (see Section 3.2.1). The Pleiades (120 Myr; Rebull et al. 2016) and Praesepe (650 Myr; Douglas et al. 2017) are shown for reference. Stars in the core and the halo of NGC 2516 overlap with the Pleiades at $(Bp-Rp)_0 < 1.2$. From $1.2 < (Bp-Rp)_0 < 1.7$, some NGC 2516 members have longer rotation periods than Pleiades members. *Bottom row:* NGC 2516 colored by binarity indicators. Sources with $RUWE > 1.2$ appear in red (astrometric binaries; 11% of stars). Overplotted in orange are sources at least 0.3 mag above an empirically fit cluster isochrone (photometric binaries; 20% of stars).

comparison against the Pleiades and Praesepe, we used the rotation periods and dereddened colors from Table 5 of [Curtis et al. \(2020\)](#), which drew on data from [Rebull et al. \(2016\)](#) and [Douglas et al. \(2019\)](#) respectively. The first order conclusion is that the Pleiades and NGC 2516 appear gyrochronologically coeval for colors spanning $0.5 < (B_p - R_p)_0 < 1.2$. The implications of this comparison for the age of NGC 2516 are discussed in Section 4.4.

The bottom row of Figure 4 shows the same data, with the points colored with indicators of binarity. To assess astrometric binarity, we used the renormalized unit weight error (RUWE) from Gaia EDR3. For plotting purposes, we labeled anything with RUWE exceeding 1.2 as an astrometric binary (11% of the overall cluster sample; see *e.g.*, [Belokurov et al. 2020](#)). To assess photometric binarity, we fitted a spline to Figure 3, fixing the nodes by hand. We then labeled any points brighter than 0.3 mag above the cluster sequence as photometric binaries. This included 20% of the overall cluster sample. Many of the resulting candidate binaries, though not all of them, appear below the slow rotation sequence. In set \mathcal{B} , over the color range where the slow and fast sequence are present ($0.5 < (B_p - R_p)_0 < 1.3$), there are 281 stars, of which 103 (37%) show signs of binarity. Dividing these 281 stars into “fast” and “slow” sequences by eye, the fraction of stars showing signs of binarity in the slow and fast subsamples are 30% (63/210) and 56% (40/71), respectively. We speculate on possible explanations in Section 4.2.

3.2.3. Comparing Kinematics and Rotation

The TESS rotation periods can provide an independent check on the Gaia-derived kinematic cluster memberships. We explored this by cross-matching the stars with detected TESS rotation periods against our original target list of 3,298 Gaia DR2 members.

To visualize the results, we again opted for Cartesian coordinates, and supplemented them by calculating the tangential stellar velocities relative to the cluster center. Appendix D discusses the projection effect correction required for calculating the tangential velocities: for a star at position (α, δ) , we compare the observed proper motion $(\mu_{\alpha'}, \mu_{\delta})$ with what the proper motion at the star’s position would have been if the star were comoving with the core of NGC 2516. This yields a quantity we denote Δv^* , per [M21](#). We convert these proper motion differences to physical units by dividing by the distance to each star, taken as the inverse parallax.

The results are shown in the top two rows of Figure 5. In these figures, to ensure a fair comparison, we only show stars with $0.5 < (B_p - R_p)_0 < 1.2$ for which our TESS pipeline succeeding in making light curves. In other words—the base sample is the stars for which we could have plausibly detected a rotation period. This color range is preferred since the the slow sequence becomes less defined for spectral types later than \approx K4V. The bins in the histograms (top-right) were chosen to ensure that the same number of stars were in each bin. Rotation periods are detected for 66% of stars at least 25 pc from the cluster core. The average detection rate inside of 25 pc, 73%, is slightly higher.

The lower panels of Figure 5 give a second view of how field star contamination affects the outskirts of the cluster. Of the outermost 100 stars in position space with detected rotation periods, ≈ 8 appear as outliers above the slow sequence, compared to just a few for the innermost 100 stars. For the outermost 100 stars in velocity space, ≈ 13 appear as outliers. After accounting for the stars that were expected to show rotation periods and did not, this suggests field contaminant rates of ≈ 40 –50% for the outermost cluster members in our target list.

Even with contaminants, our rotation period measurements show that the halo extends to separations of ≈ 250 pc in physical space from the cluster core. The most widely separated F2V-K2V stars with rotation periods (blue points in Figure 5) are separated by ≈ 430 pc. The total length of the structure is therefore 400–500 pc, depending on which members of the halo are chosen as the “tips” on either end. This agrees with the overall structure of the halo reported by [KC19](#), with some minor caveats visible in the top-left panels of Figure 5.

In projection-corrected tangential velocity space, the fraction of stars with rotation period detections remains high out to roughly 5 km s^{-1} . [Meingast et al. \(2021\)](#) by comparison required a physically motivated cut in tangential velocity space of 1.5 km s^{-1} . Our results show that at the expense of higher field star contamination rates, bona fide members can be identified even out at higher velocity separations.

3.3. Lithium from Gaia-ESO and GALAH

The third and final approach we took for confirming the youth of the halo population of NGC 2516 was an analysis of the Li I 6708 Å doublet. The method has been reviewed by [Soderblom \(2010\)](#), and its connection to stellar rotation has recently been surveyed by [Bouvier \(2020\)](#). For NGC 2516, two spectroscopic datasets seemed particularly important: Gaia-ESO ([Gilmore et al. 2012](#)) and GALAH ([Silva et al. 2015](#)). At the time of analysis, Gaia-ESO DR4 and GALAH DR3 were the most relevant, respectively (*e.g.*, [Randich et al. 2018](#); [Buder et al. 2020](#)). The target selection and results from each survey were as follows.

Gaia-ESO selected candidate NGC 2516 members to observe with the GIRAFFE and UVES spectrographs based on previously reported literature members and publicly available photometry. Since the existence of the NGC 2516 halo was not known at the time of target selection, very few “halo” stars are in the sample. For NGC 2516, [Randich et al. \(2018\)](#) ultimately reported stellar parameters (including lithium equivalent widths and metallicities) for 796 stars that they considered possible NGC 2516 members. Cross-matching against our kinematic list of 3,298 candidate members by position and imposing a $0.^{\circ}5$ maximum separation limit yields 492 kinematic members for which a Gaia-ESO spectrum was acquired and stellar parameters were reported. 15 of these (all with $(B_p - R_p)_0 > 2.0$) are spurious matches based on the Gaia color and GES effective temperature, and we remove them. This yields 477 stars, of which 436 are in the core, and 41 are in the halo. The lop-sided ratio is due to the Gaia-ESO selection function. We verified by directly

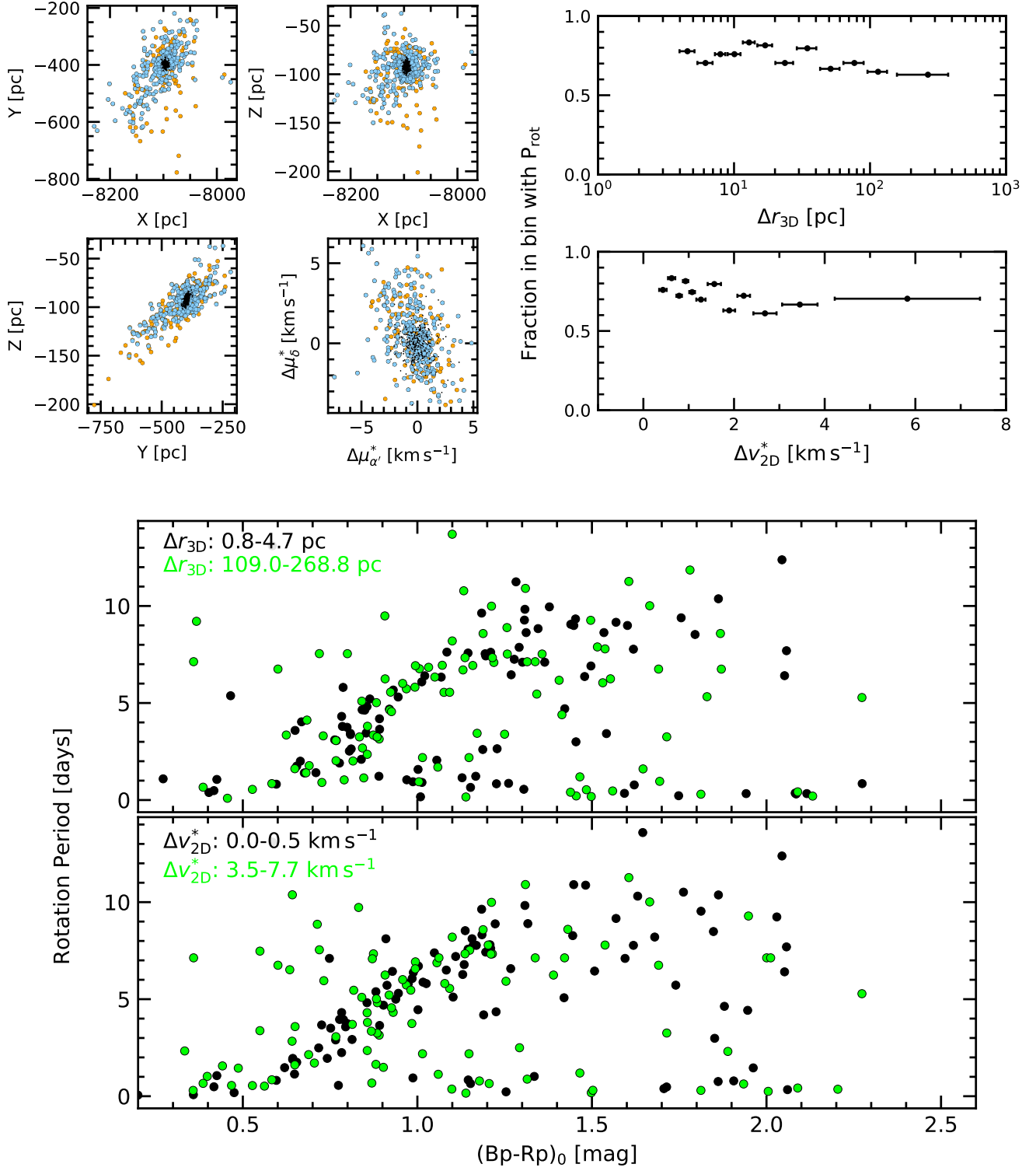


Figure 5. Members of NGC 2516 exist hundreds of parsecs from the core, and up to $\approx 5 \text{ km s}^{-1}$ from the core in tangential velocity. Top left: Cartesian positions (as in Figure 2) and 2D-tangential velocities for halo members that meet kinematic membership criteria (Subset \mathcal{A}). Stars with detected rotation periods are shown in blue; halo members for which rotation periods should have been detectable, but were not detected, are shown in orange. Stars in the core are shown as black points. Computing the 2D-tangential velocity requires a correction for projection effects (Appendix D). In the top right, the histograms on bin versus 3D separation from the core and 2D tangential velocity difference. Bin widths are chosen to enforce the same number of stars in the denominator ($N = 54$) per bin. In the bottom panels, the innermost and outermost 100 stars in position and velocity space are displayed in the space of rotation periods and dereddened colors.

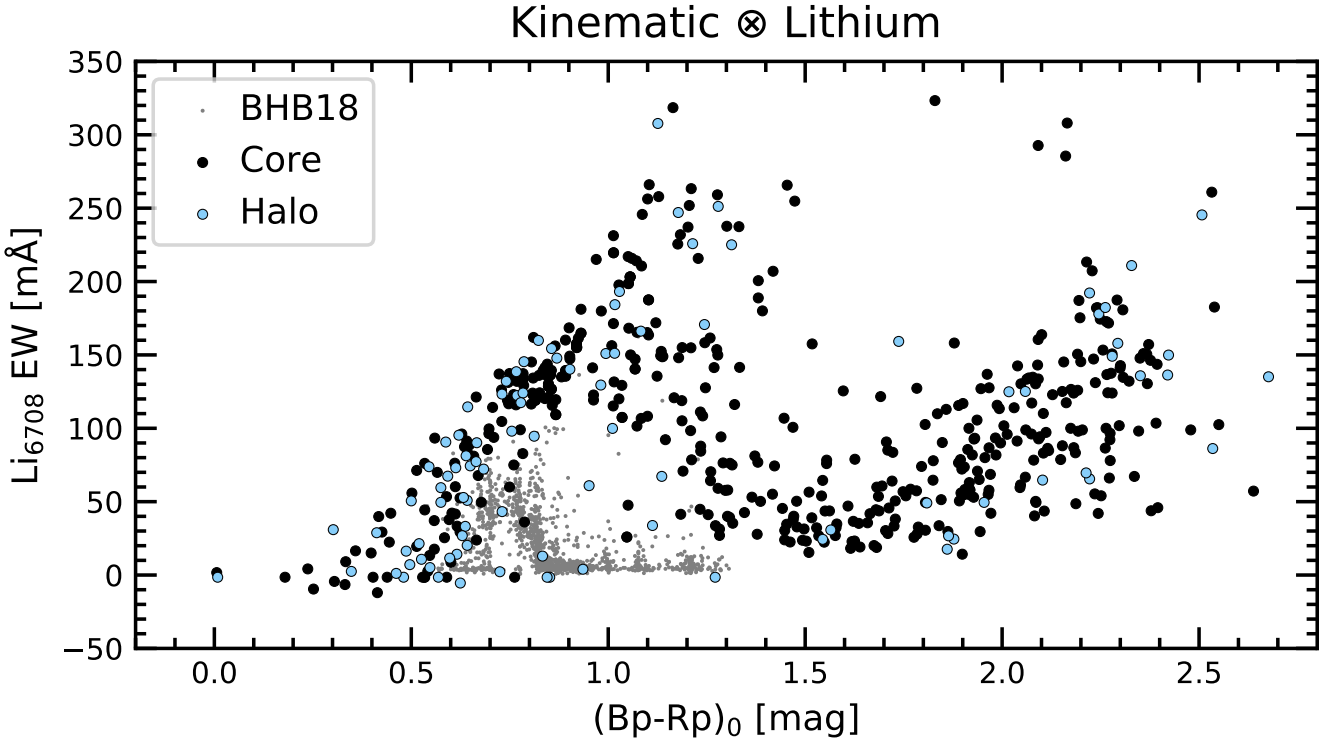


Figure 6. Lithium in the core and halo of NGC 2516. Equivalent width of the 6708 Å doublet is shown versus dereddened color for all kinematic NGC 2516 members with Gaia-ESO ($N = 452$) or GALAH ($N = 107$) spectra available. The GALAH spectra comprise slightly over half of the halo stars, due to the non-targeted selection function of that survey. The gray points are Keck-HIRES measurements of stars with detected transiting planets from the Kepler mission (Berger et al. 2018). Points with $\text{EW} \approx 0 \text{ m}\text{\AA}$ are non-detections.

querying the ESO archive that Randich et al. (2018) indeed included $> 99\%$ of the available Gaia-ESO spectra as part of their NGC 2516 sample, and so we opted to use their results rather than repeating their analysis.

The GALAH DR3 target selection is discussed in depth by Buder et al. (2020). The relevant aspects for our analysis are that the “main” survey targeted $12 < V < 14$ stars at $\delta < +10^\circ$, provided the stars were at least ten degrees from the galactic plane. The survey is spatially inhomogeneous⁶. Special targeting for stars in the TESS southern continuous viewing zone, and for known open cluster members was also performed. We identified the candidate NGC 2516 members for which spectra had been obtained by searching the GALAH_DR3_main_allstar_v1 catalog, after excluding stars with the stellar parameter bit flags 1, 2, 3. This excludes spectra with unreliable broadening, low S/N, and unreliable wavelength solutions (see Table 6 of Buder et al. 2020). Since our main focus is measuring equivalent widths for the Li 6708 Å doublet, these were the most relevant bit flags. Of our 3,298 candidate NGC 2516 members, 107 had spectra in GALAH DR3. 51 were in the “core”; 56 were in the “halo”. 78 had “finite” lithium, i.e., no lithium flag set.

We downloaded⁷ the GALAH DR3 spectra for all 107 entries. We then measured the lithium equivalent widths using the `specutils` package (Earl et al. 2020). We did this by first focusing in on a 15 Å window centered on the 6707.835 Å lithium doublet. We then continuum normalized the spectra using a third-degree Chebyshev series, while excluding any regions that showed absorption lines (e.g., Fe I is present at 6703.58 Å and 6705.10 Å). We proceeded by fitting a Gaussian to the continuum normalized spectra, considering only a ± 1 Å window centered on the Li doublet. The equivalent widths were then evaluated by numerically integrating the fitted model over the same window. Our approach therefore includes the Fe 6707.44 blend in the reported Li equivalent widths—which leads to systematic overestimates of ≈ 10 to 15 mÅ (e.g., Bouvier et al. 2018). Finally, to derive uncertainties on the EWs, we repeated the procedure twenty times, but added noise to the spectra, drawn from a normal distribution with a scale set by the standard deviation of the continuum. The reported uncertainties are then drawn from the 84th and 16th percentiles of the resulting EW distribution. We verified the overall scale of our results by comparing the 21 stars that overlapped between GALAH and Gaia-ESO. 17 of the 21 measurements agreed within $1-\sigma$. The remaining

⁶ See the footprint at <https://www.galah-survey.org/news/announcing-galah-dr3>

⁷ Via datacentral.org.au/services/download, using the `sobject_id` identifiers.

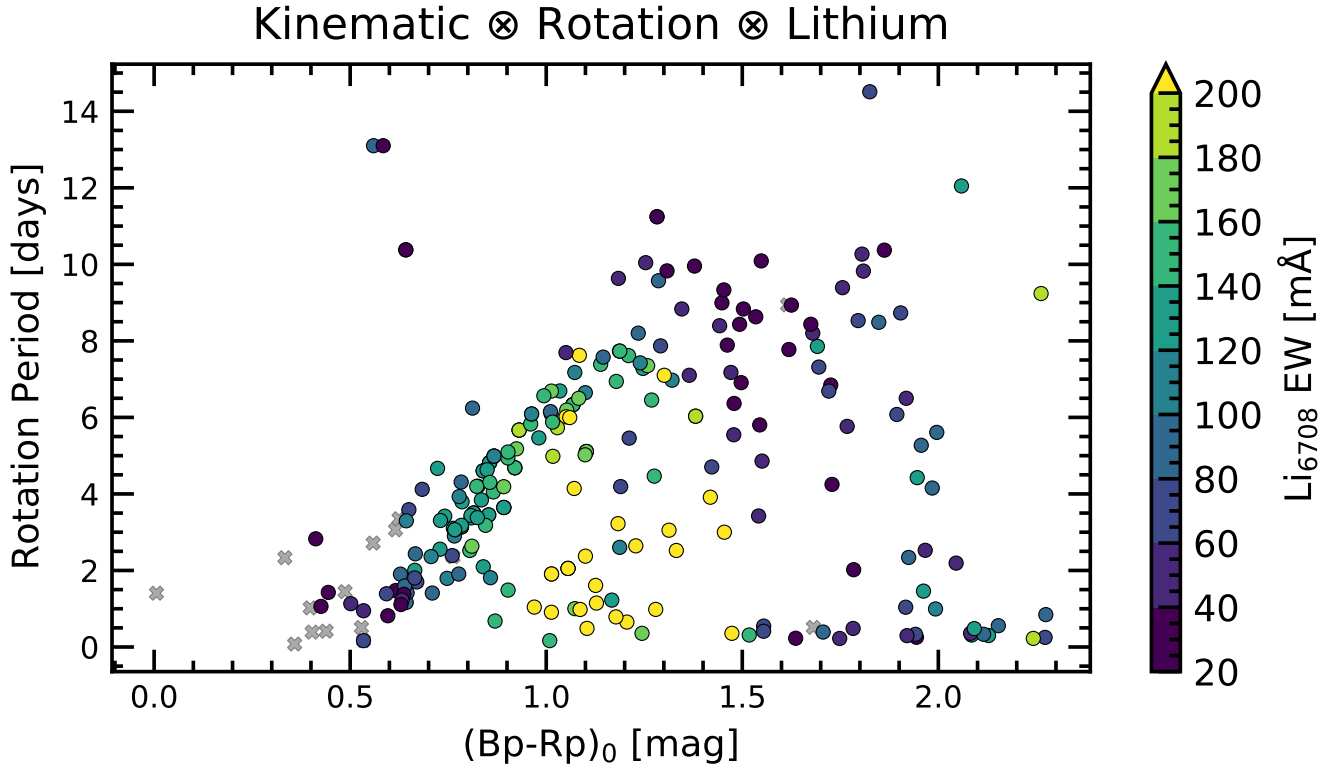


Figure 7. Lithium and rotation in NGC 2516. Points show all kinematic NGC 2516 members with TESS rotation periods in the Gaia-ESO or GALAH surveys, and are colored by equivalent width. Points with reported equivalent widths below $20\text{ m}\text{\AA}$ (including non-detections) are shown with gray crosses. The lithium-rotation correlation for the K-dwarfs has been observed in other young clusters, and is discussed in Section 3.3.

four were stars with $T_{\text{eff}} > 6200\text{ K}$, for which Randich et al. (2018) reported Li EW detections ranging from 50 to $75\text{ m}\text{\AA}$, and for which we found either null results or only slightly significant ($\approx 30\text{ m}\text{\AA}$) detections.

Figure 6 shows the concatenation of the Gaia-ESO and GALAH results, with the points colored by whether the stars are in the core or the halo of the cluster. The GALAH spectra span a color range of $0 < (Bp - Rp)_0 < 1.5$, due to the $V < 14$ brightness cutoff of the survey. The overall increase of Li EW from $0 < (Bp - Rp)_0 < 1.0$ is thought to be driven by the temperatures in the stellar chromospheres: hotter stars fully ionize Li out of its ground state (e.g., Figure 4 of Soderblom et al. 1993). The depletion of stars redder than $(Bp - Rp)_0 \gtrsim 1.4$, i.e., later than K4.5V ($0.71 M_{\odot}$), is visible relative to the earlier K dwarfs. For comparison, we have also plotted the Li EWs measured by Berger et al. (2018) for planet-hosting stars in the Kepler field (we interpolated from their effective temperatures using the Pecaut & Mamajek (2013) table⁸. The field star distribution peaks at late F-type stars. The majority of kinematically selected stars in the core and the halo show lithium equivalent widths substantially in excess of these field stars.

We can go one step further, and match our sample of kinematically selected stars with spectra against the TESS rotators. The result is shown in Figure 7. At fixed stellar mass, the rapid rotators have lithium equivalent widths an order of magnitude larger than the slow rotators. This effect is mostly apparent in the K dwarfs. Similar trends were noted in the Pleiades over three decades ago (Butler et al. 1987), and are most likely caused by intrinsic differences in lithium abundance (Soderblom et al. 1993). Alternative explanations, such as differences in line-formation conditions (e.g., chromospheric temperatures, microturbulent velocities, or the presence of starspots) are incompatible with the available data. The lithium-rotation correlation is discussed further below (Section 4.3).

4. DISCUSSION

4.1. How did the halo form?

Any theory for the structure of NGC 2516, the Psc Eri stream, and the strings and halos found by KC19 and M21 needs to explain a few observations. First is their aspect ratios. The halo of NGC 2516, for instance, extends over at least 500 pc, despite being only ≈ 25 pc wide. Second is their axial tilts in the plane of the Milky Way – why their leading and trailing arms tend to conform to the Galaxy’s differential rotation (e.g., Figure 2 or Figure 13 of M21). Third is the correlation between the mean LSR-subtracted cluster ve-

⁸ http://www.pas.rochester.edu/~emamajek/EEM_dwarf_UBVIJHK_colors_Teff.txt, version 2019.3.22.

locity and elongation axes (blue arrows in Figure 2). Such a correlation has also been noted in Coma Ber by Tang et al. (2019). The other halos may show similar trends.

One possible explanation is that these structures are tidal tails (*e.g.*, Krumholz et al. 2019). The idea would be that stars escape out of the Lagrange points imposed by the Milky Way’s potential, and then form leading and lagging arms due to differential rotation in the Galaxy. In this context, Psc Eri for instance might represent the completion of a process that NGC 2516 is still undergoing.

A second possibility is that the clusters form in larger and more dispersed star formation complexes: the stars in the halo need not have formed in the same “clump” as those in the cluster core. In other words, the formation environment might be better described a giant molecular filament, rather than a giant molecular cloud. A sample of such filaments has recently been collected and analyzed by Zucker et al. (2018): if the current $\approx 20:1$ aspect ratio of NGC 2516 were primordial, its structure would match the aspect ratios of what they term either “elongated dense core complexes”, or “bone candidates”. A more immediate example is the Orion A cloud. Großschedl et al. (2018) showed using young stellar objects as tracers that Orion A is 90 pc long, and that it has a dense “head” and a lower density “tail”.

One way to rule between the two possibilities would be to observationally establish an age-size correlation. If the ≈ 100 Myr halos are produced primarily through evaporation and expansion, then the younger clusters should be significantly smaller. A theoretical approach along similar lines would be to perform a dynamical analysis of whether filaments like Orion A, or those in the Zucker et al. (2018) sample, are at all expected to evolve into structures resembling NGC 2516.

4.2. Rotation at 100-200 Myr

From their rotation period analysis of NGC 2516, Fritzewski et al. (2020) have recently demonstrated that at ages between 100 and 200 Myr, young clusters (NGC 2516, Blanco 1, the Pleiades, Psc Eri, M 35, and M 50) all show similar rotation period distributions. The FGK stars show a “slow sequence”, a population of “rapid rotators”, and in some cases stars in the “void” between the two populations (*e.g.*, Psc Eri and NGC 2516 show more stars in the void than the Pleiades). The late M dwarfs with detected rotation periods tend to rotate very rapidly (< 3 days), although these are beyond the magnitude limit of our analysis. This section briefly discusses the origins of these features in the rotation-color diagram.

The existence of a slow sequence is the main premise of gyrochronology (*e.g.*, Barnes 2003). While the initial spin-down relation ($P_{\text{rot}} \sim t^{1/2}$) proposed by Skumanich (1972) has not worked in detail, the general idea is correct, and the first-order effect can be understood through magnetic breaking (Weber & Davis 1967).

The other features of the rotation-color diagram are indications that magnetic breaking is not always the most important effect. The question of why the rapid rotators exist,

for instance, has not yet been definitively answered. Models that introduce variable core-envelope decoupling timescales can reproduce each type of population (Irwin et al. 2007), but the question then shifts to why these decoupling timescales should be differ for stars that are otherwise identical. Another possible explanation invokes a spontaneous and random change of magnetic field topology that causes the dynamo to couple more strongly with the stellar wind (Brown 2014). Other processes could be external the star entirely: Qureshi et al. (2018) for instance have reported that mergers between giant planets and the star could explain a non-negligible fraction of the rapid rotators.

A separate hypothesis that we can test using the existing data is the idea that rapid rotation can be explained through binarity. Analyses by *e.g.*, Gillen et al. (2020) and Simonian et al. (2019) have reported that rapid rotation in young clusters and in the field is correlated with binarity. Related effects could include tidal synchronization for the shortest period binaries, or alternatively disk truncation that when combined with magnetic locking (CITE) could produce the rotation period bimodality.

The lower panels of Figure 4 show our attempt at identifying unresolved binaries in the NGC 2516 rotation sample. Binaries resolved by Gaia were already excluded in our initial definitions of the samples. In NGC 2516 we see that the fraction of stars showing signs of binarity in the slow and fast rotation subsamples are 30% (63/210) and 56% (40/71); the fast rotators show a preference for binarity. This correlation is in line with the earlier findings noted above, though we emphasize many rapid rotators in NGC 2516 (34%) have no evidence for being binary.

Comparing the explanations of disk-locking against tidal synchronization, the population statistics do seem to strain the possibility of tidal synchronization. A quarter of the NGC 2516 members are rapidly rotating. In comparison, in the field half of Sun-like stars are binaries, and $\approx 9\%$ have periods below 100 days (Raghavan et al. 2010). If we assume that all binaries with sub-100 day periods become tidally synchronized, we can only explain a rapid rotator occurrence rate of $\approx 5\%$.

A separate effect is that on the slow rotation sequence, Figure 4 shows that the binary stars appear to be either preferentially redder, or to have faster rotation periods than the single stars. One likely explanation for this could be that the unresolved binaries have a component contributing additional red light to the system, skewing the color measurement of the primary. Whether any physical effects could be at play remains a question for future work.

4.3. The lithium-rotation correlation

The lithium-rotation correlation (Figure 7) has been shown to carry over beyond just equivalent widths, and to the actual abundance of lithium in the photosphere, A(Li). Soderblom et al. (1993) calculated the relevant LTE curves of growth for the Li 6708 Å doublet, and used them to convert our measured equivalent widths to abundances. Non-LTE corrections affect the abundances by < 0.5 dex and do not significantly

affect the global relation between Li abundance and stellar temperature or rotation (Carlsson et al. 1994; Lind et al. 2009).

More recent studies of lithium and rotation since Soderblom et al. (1993) have expanded these results in the Pleiades, the Psc-Eri stream, and M 35, among other clusters (Bouvier et al. 2018; Arancibia et al. 2020; Jeffries et al. 2020). In NGC 2516 specifically, Jeffries et al. (1998) observed a similar trend that that seen in Figure 7 when analyzing 24 stars in the core of NGC 2516. Our concatenation of the Randich et al. (2018) Gaia-ESO results with the GALAH-DR3 spectra represent a significant expansion in volume and color range since these earlier studies.

What causes the correlation between lithium abundance and rotation at fixed stellar mass? **FIXME: improve this paragraph** Processes both internal and external to the star have been suggested to explain the lithium-rotation trend (CITE see the recent review by Bouvier+20). One explanation based in the stellar interior could be that the convective mixing efficiency is anticorrelated with the surface rotation (e.g., CITE Siess + Livio 1997, Baraffe+2017). Another possibility could be that stronger magnetic fields in the star’s interior inhibit convection (READ e.g., Ventura+98, Chabrier+07, Somers + Pinsonneault 2014). An external process that might also be important is the effect of star-disk magnetic locking during the PMS phase (CITE: magnetic braking). Longer disk lifetimes would lead to the star’s outer convective zone being locked for longer while the radiative core contracts. The resulting differential rotation and rotational mixing could drive the lithium depletion (CITE: Bouvier 08, Eggenberger+12). We have no preference between these possibilities—we simply note that the NGC 2516 sample could be another helpful data point in distinguishing them.

4.4. Age of NGC 2516

Cummings & Kalirai (2018) favor 150 Myr based on MSTO. Godoy-Rivera+2021 favor 150 Myr... based on ...? what? "" Similar to Cummings et al. (2016), Cummings & Kalirai (2018), and Cummings et al. (2018) (see also Fritzevski et al. 2020 and Healy & McCullough 2020) """

Gyrochronological Age—Comparing the slow sequence of the Pleiades and NGC 2516 more closely, the top row of Figure 4 shows that the two sequences overlap from $0.5 < (B_p - R_p)_0 < 1.2$. At redder colors ($1.2 < (B_p - R_p)_0 < 1.7$) the dispersion in rotation periods increases. The maximum rotation periods seen in NGC 2516 across both sets \mathcal{A} and \mathcal{B} extend up to ≈ 11 days, rather than the ≈ 8.5 day upper limit seen in the Pleiades. This is consistent with NGC 2516 being slightly older than the Pleiades.

Fitting a model to substantiate the claim that NGC 2516 is gyrochronologically older than the Pleiades (e.g., any of Majajek & Hillenbrand 2008; Angus et al. 2019; Spada & Lanzafame 2020) is, unfortunately, an exercise in tautology. The aforementioned models are empirically calibrated using the Pleiades and Praesepe. In other words, at $(B_p - R_p)_0 = 1.35$,

we observe rotation periods in NGC 2516 ranging from 7 to 10 days. The 7 day rotation periods are consistent with those observed in the Pleiades; the 10 day rotation periods are not. Fitting formulae from the previously cited studies give ages for a star with $\{(B_p - R_p)_0 = 1.35, (B - V)_0 = 1.10, P = 7 \text{ day}\}$ of 204 Myr, 316 Myr, and 107 Myr respectively. Therefore, only the Spada & Lanzafame (2020) model has an absolute scale that is well-calibrated at these ages and colors. For an 8 day rotation period of a star with the same color, this model quotes a 193 Myr age; at 9 days, 388 Myr. Given this degree of model uncertainty, we prefer the relative statement that NGC 2516 appears slightly gyrochronologically older than the Pleiades, and much younger than Praesepe. Given a Pleiades age of 130 ± 15 Myr (an average of MSTO and rotation-corrected lithium-depletion results; Cummings & Kalirai 2018), a gyrochronology-derived age estimate for NGC 2516 between 150 and 200 Myr would therefore appear reasonable. Much older, and the issue of why the F and G dwarfs do not spin down becomes pressing.

5. CONCLUSION

The combination of astrometry from Gaia, photometry from TESS, and spectroscopy from GALAH and Gaia-ESO has clarified a few things about the structure of NGC 2516.

- *Over-densities observed in the Gaia 3-D positions and 2-D velocities revealed a halo of stars spanning ≈ 500 parsecs in the plane of the galaxy.* The earliest reference to this halo that we can find is by Kounkel & Covey (2019). The halo is more precisely described as a leading and trailing tail (Figure 2), with the leading edge angled toward the galactic center, relative to the cluster’s orbit in the Galaxy. This is consistent with the direction and amplitude of the Milky Way’s differential rotation ($\approx 0.2 \text{ deg Myr}^{-1} \text{ kpc}^{-1}$), and similar halos/tails have been observed around ≈ 10 other nearby open clusters (Meingast et al. 2021).
- *Isochronal, rotational, and lithium dating show that the halo of NGC 2516 is coeval with its core.* In short, all the data are consistent with the halo being real. The Gaia EDR3 photometry and astrometry show a main-sequence turnoff that suggest an isochronal age of 150 Myr for both the core and halo (Figure 3). The faintest M dwarfs in the core and halo are also brighter than comparison field stars of the same color. Gyrochronally, stars in NGC 2516 spanning $0.5 < (B_p - R_p)_0 < 1.2$ (spectral types F2V-K3V) overlap with the slow sequence of the Pleiades (Figure 4). At redder colors, from $1.2 < (B_p - R_p)_0 < 1.7$ (spectral types K3V-K6V, $M_* \approx 0.6\text{--}0.7 M_\odot$), there is a larger dispersion in rotation period. The upper envelope of the rotation period distribution at these redder colors extends to longer rotation periods than in the Pleiades (11 vs. 8 day rotation periods). This is consistent with NGC 2516 being slightly older than the Pleiades (i.e., ≈ 150 Myr). The lithium equivalent widths of the kine-

matic cluster members (Figure 6) are consistent with this assessment.

- *Bonafide NGC 2516 members exist out to ≈ 250 pc in separation and out to ≈ 5 km s $^{-1}$ in tangential velocity separation from the cluster core.* Figure 5 shows the overlap between kinematic and rotational cluster members used to make this assessment.
- *The field star contamination rate increases at larger physical and velocity separations from the cluster core.* The right and lower panels of Figure 5 quantify the statement: $\approx 75\%$ of the “inner-most” members have detected rotation periods. This fraction decreases to $\approx 60\%$ at physical separations of ≈ 200 pc. Based on the rate at which rotation periods are detected at or underneath the gyrochronological slow sequence, field stars appear to contaminate the outermost candidate cluster members at a rate between 40% and 50%. Given the number density ratios of cluster to field stars at these wide separations ($\approx 10^{-3}$, Meingast et al. 2021), these contamination fractions are not as bad as one might fear.
- *The rapid rotators show elevated lithium abundances, and elevated binarity fractions.* Each trend has been noted in comparable stellar populations (e.g., Soderblom et al. 1993, Gillen et al. 2020). The rough orders of magnitude of the effects are ≈ 1 dex in lithium abundance for a factor of 10 in rotation period, and a factor of $\approx 2 \times$ enhancement in binarity fraction for fast vs. slowly rotating G and early K dwarfs.

The existence of the halo itself should not be not very surprising. A star with a 1 km s $^{-1}$ velocity difference from the cluster average will move away from the center at a rate of 1 pc Myr $^{-1}$. For a ~ 100 Myr old cluster, a halo with characteristic size ~ 100 pc is therefore expected, given that the typical velocity dispersions of open clusters are of the order of kilometers per second.

On the other hand, our ability to reliably identify members of these halos is rather surprising. These stars have remained hidden in the background of the Galaxy throughout centuries of modern astronomy. The consequences that these halo stars will have in expanding our understanding of planetary and stellar origins are only just beginning to be understood.

ACKNOWLEDGMENTS

The authors thank X and Y for fruitful discussions.

B. Tofflemire,

L.G.B. and J.H. acknowledge support by the TESS GI Program, program NUMBER, through NASA grant NUMBER. L.G.B. was also supported by a XXXX Fellowship from Princeton University. This study was based in part on observations at Cerro Tololo Inter-American Observatory at

NSF’s NOIRLab (NOIRLab Prop. ID 2020A-0146; 2020B-NUMBER PI: L. Bouma), which is managed by the Association of Universities for Research in Astronomy (AURA) under a cooperative agreement with the National Science Foundation. ACKNOWLEDGE PFS / CAMPANAS. This paper includes data collected by the TESS mission, which are publicly available from the Mikulski Archive for Space Telescopes (MAST). Funding for the TESS mission is provided by NASA’s Science Mission directorate. We thank the TESS Architects (George Ricker, Roland Vanderspek, Dave Latham, Sara Seager, Josh Winn, Jon Jenkins) and the many TESS team members for their efforts to make the mission a continued success.

Software: astrobase (Bhatti et al. 2018), astropy (Astropy Collaboration et al. 2018), astroquery (Ginsburg et al. 2018), cdips-pipeline (Bhatti et al. 2019), corner (Foreman-Mackey 2016), gala (Price-Whelan 2017; Price-Whelan et al. 2017), IPython (Pérez & Granger 2007), matplotlib (Hunter 2007), numpy (Walt et al. 2011), pandas (McKinney 2010), scipy (Jones et al. 2001), wotan (Hippke et al. 2019).

Facilities: Astrometry: Gaia (Gaia Collaboration et al. 2016, 2018). Imaging: Second Generation Digitized Sky Survey, SOAR (HRCam; Tokovinin 2018). Spectroscopy: CTIO1.5m (CHIRON; Tokovinin et al. 2013), Photometry: TESS (Ricker et al. 2015).

REFERENCES

- Adams, F. C. 2010, *ARA&A*, **48**, 47, publisher: Annual Reviews
- Angus, R., Morton, T. D., Foreman-Mackey, D., et al. 2019, *AJ*, **158**, 173
- Arancibia, J., Bouvier, J., Bayo, A., et al. 2020, Boletin de la Asociacion Argentina de Astronomia La Plata Argentina, 61C, 81
- Astropy Collaboration, Price-Whelan, A. M., Sipőcz, B. M., et al. 2018, *AJ*, **156**, 123
- Bailey, J. I., Mateo, M., White, R. J., Shectman, S. A., & Crane, J. D. 2018, *MNRAS*, **475**, 1609
- Baratella, M., D’Orazi, V., Carraro, G., et al. 2020, *A&A*, **634**, A34
- Barnes, S. A. 2003, *ApJ*, **586**, 464
- Belokurov, V., Penoyre, Z., Oh, S., et al. 2020, arXiv:2003.05467 [astro-ph]
- Berger, T. A., Howard, A. W., & Boesgaard, A. M. 2018, *ApJ*, **855**, 115
- Bergond, G., Leon, S., & Guibert, J. 2001, *A&A*, **377**, 462
- Bhatti, W., Bouma, L., & Yee, S. 2019, cdips-pipeline v0.1.0, <https://doi.org/10.5281/zenodo.3370324>
- Bhatti, W., Bouma, L. G., & Wallace, J. 2018, astrobase, <https://doi.org/10.5281/zenodo.1469822>
- Bonifacio, P., Monai, S., & Beers, T. C. 2000, *AJ*, **120**, 2065
- Bouma, L. G., Hartman, J. D., Bhatti, W., Winn, J. N., & Bakos, G. Á. 2019, *ApJS*, **245**, 13
- Bouvier, J. 2020, arXiv:2009.02086 [astro-ph], arXiv: 2009.02086
- Bouvier, J., Barrado, D., Moraux, E., et al. 2018, *A&A*, **613**, A63
- Bovy, J. 2015, *The Astrophysical Journal Supplement Series*, **216**, 29
- Bressan, A., Marigo, P., Girardi, L., et al. 2012, *MNRAS*, **427**, 127
- Brown, T. M. 2014, *ApJ*, **789**, 101
- Buder, S., Sharma, S., Kos, J., et al. 2020, arXiv e-prints, 2011, arXiv:2011.02505
- Butler, R. P., Cohen, R. D., Duncan, D. K., & Marcy, G. W. 1987, *ApJL*, **319**, L19
- Cantat-Gaudin, T., Jordi, C., Vallenari, A., et al. 2018, *A&A*, **618**, A93
- Cantat-Gaudin, T., Jordi, C., Wright, N. J., et al. 2019, *A&A*, **626**, A17
- Carlsson, M., Rutten, R. J., Bruls, J. H. M. J., & Shchukina, N. G. 1994, *A&A*, **288**, 860
- Chen, Y., Bressan, A., Girardi, L., et al. 2015, *MNRAS*, **452**, 1068
- Chen, Y., Girardi, L., Bressan, A., et al. 2014, *MNRAS*, **444**, 2525
- Chen, Y., Girardi, L., Fu, X., et al. 2019, *A&A*, **632**, A105
- Choi, J., Dotter, A., Conroy, C., et al. 2016, *ApJ*, **823**, 102
- Cummings, J. 2011, PhD thesis, Indiana University
- Cummings, J. D., & Kalirai, J. S. 2018, *AJ*, **156**, 165
- Curtis, J. L., Agüeros, M. A., Mamajek, E. E., Wright, J. T., & Cummings, J. D. 2019, *AJ*, **158**, 77
- Curtis, J. L., Agüeros, M. A., Matt, S. P., et al. 2020, *ApJ*, **904**, 140
- Davenport, J. R. A., & Sandquist, E. L. 2010, *ApJ*, **711**, 559
- de Zeeuw, P. T., Hoogerwerf, R., de Bruijne, J. H. J., Brown, A. G. A., & Blaauw, A. 1999, *AJ*, **117**, 354
- Douglas, S. T., Agüeros, M. A., Covey, K. R., & Kraus, A. 2017, *ApJ*, **842**, 83
- Douglas, S. T., Curtis, J. L., Agüeros, M. A., et al. 2019, *ApJ*, **879**, 100
- Earl, N., Tollerud, E., Jones, C., et al. 2020, astropy/specutils
- Feiden, G. A., & Chaboyer, B. 2013, *ApJ*, **779**, 183
- Foreman-Mackey, D. 2016, *Journal of Open Source Software*, **1**, 24
- Freeman, K., & Bland-Hawthorn, J. 2002, *ARA&A*, **40**, 487
- Fritzewski, D. J., Barnes, S. A., James, D. J., & Strassmeier, K. G. 2020, *A&A*, **641**, A51
- Fukushige, T., & Heggie, D. C. 2000, *MNRAS*, **318**, 753
- Fürnkranz, V., Meingast, S., & Alves, J. 2019, *A&A*, **624**, L11
- Gagné, J., & Faherty, J. K. 2018, *ApJ*, **862**, 138
- Gagné, J., Faherty, J. K., & Popinchalk, M. 2020, *Res. Notes AAS*, **4**, 92
- Gagné, J., Roy-Loubier, O., Faherty, J. K., Doyon, R., & Malo, L. 2018, *ApJ*, **860**, 43
- Gagné, J., David, T. J., Mamajek, E. E., et al. 2020, *ApJ*, **903**, 96
- Gaia Collaboration, Prusti, T., de Bruijne, J. H. J., et al. 2016, *A&A*, **595**, A1
- Gaia Collaboration, Brown, A. G. A., Vallenari, A., et al. 2018, *A&A*, **616**, A1
- Gillen, E., Briegal, J. T., Hodgkin, S. T., et al. 2020, *MNRAS*, **492**, 1008
- Gilmore, G., Randich, S., Asplund, M., et al. 2012, *The Messenger*, **147**
- Ginsburg, A., Sipocz, B., Madhura Parikh, et al. 2018, Astropy/Astroquery: V0.3.7 Release
- Großschedl, J. E., Alves, J., Meingast, S., et al. 2018, *A&A*, **619**, A106
- Hippke, M., David, T. J., Mulders, G. D., & Heller, R. 2019, *AJ*, **158**, 143
- Hogg, D. W., Casey, A. R., Ness, M., et al. 2016, *The Astrophysical Journal*, **833**, 262
- Hunt, E. L., & Reffert, S. 2020, *A&A*, arXiv: 2012.04267
- Hunter, J. D. 2007, Computing in Science & Engineering, **9**, 90
- Irwin, J., Hodgkin, S., Aigrain, S., et al. 2007, *MNRAS*, **377**, 741
- Jeffries, R. D., Jackson, R. J., Sun, Q., & Deliyannis, C. P. 2020, *MNRAS*, **500**, 1158, arXiv: 2010.04217
- Jeffries, R. D., James, D. J., & Thurston, M. R. 1998, *MNRAS*, **300**, 550
- Jeffries, R. D., Thurston, M. R., & Hambley, N. C. 2001, *A&A*, **375**, 863, number: 3 Publisher: EDP Sciences
- Jones, E., Oliphant, T., Peterson, P., et al. 2001, Open source scientific tools for Python

- Kharchenko, N. V., Piskunov, A. E., Schilbach, E., Röser, S., & Scholz, R.-D. 2013, *A&A*, 558, A53
- Kounkel, M., & Covey, K. 2019, *AJ*, 158, 122
- Kounkel, M., Covey, K., & Stassun, K. G. 2020, *AJ*, 160, 279
- Kounkel, M., Covey, K., Suárez, G., et al. 2018, *AJ*, 156, 84
- Krumholz, M. R., McKee, C. F., & Bland-Hawthorn, J. 2019, *ARA&A*, 57, 227
- Lada, C. J., & Lada, E. A. 2003, *ARA&A*, 41, 57
- Lamers, H. J. G. L. M., Baumgardt, H., & Gieles, M. 2010, *MNRAS*, 409, 305
- Lind, K., Asplund, M., & Barklem, P. S. 2009, *A&A*, 503, 541
- Lomb, N. R. 1976, *Astrophysics and Space Science*, 39, 447
- Mamajek, E. E., & Hillenbrand, L. A. 2008, *ApJ*, 687, 1264
- Mann, A. W., Gaidos, E., & Ansdell, M. 2013, *ApJ*, 779, 188
- Marigo, P., Girardi, L., Bressan, A., et al. 2017, *ApJ*, 835, 77
- McKinney, W. 2010, in Proceedings of the 9th Python in Science Conference, ed. S. van der Walt & J. Millman, 51
- Meingast, S., & Alves, J. 2019, *A&A*, 621, L3
- Meingast, S., Alves, J., & Fürnkranz, V. 2019, *A&A*, 622, L13
- Meingast, S., Alves, J., & Rottensteiner, A. 2021, *A&A*, 645, A84
- Ness, M., Rix, H.-W., Hogg, D. W., et al. 2018, *The Astrophysical Journal*, 853, 198
- O'Donnell, J. E. 1994, *ApJ*, 422, 158
- Oh, S., Price-Whelan, A. M., Hogg, D. W., Morton, T. D., & Spergel, D. N. 2017, *AJ*, 153, 257
- Pecaut, M. J., & Mamajek, E. E. 2013, *ApJS*, 208, 9
- Pecaut, M. J., & Mamajek, E. E. 2016, *MNRAS*, 461, 794
- Pérez, F., & Granger, B. E. 2007, *Computing in Science and Engineering*, 9, 21
- Piskunov, A. E., Just, A., Kharchenko, N. V., et al. 2018, *Astronomy and Astrophysics*, 614, A22
- Price-Whelan, A., Sipocz, B., Major, S., & Oh, S. 2017, adrn/gala: v0.2.1
- Price-Whelan, A. M. 2017, *The Journal of Open Source Software*, 2
- Qureshi, A., Naoz, S., & Shkolnik, E. L. 2018, *ApJ*, 864, 65
- Raghavan, D., McAlister, H. A., Henry, T. J., et al. 2010, *ApJS*, 190, 1
- Rajpurohit, A. S., Reylé, C., Allard, F., et al. 2013, *A&A*, 556, A15
- Randich, S., Tognelli, E., Jackson, R., et al. 2018, *A&A*, 612, A99
- Rebull, L. M., Stauffer, J. R., Bouvier, J., et al. 2016, *AJ*, 152, 113
- Ricker, G. R., Winn, J. N., Vanderspek, R., et al. 2015, *Journal of Astronomical Telescopes, Instruments, and Systems*, 1, 014003
- Röser, S., Schilbach, E., & Goldman, B. 2019, *A&A*, 621, L2
- Scargle, J. D. 1982, *ApJ*, 263, 835
- Schlaflly, E. F., & Finkbeiner, D. P. 2011, *ApJ*, 737, 103
- Schlegel, D. J., Finkbeiner, D. P., & Davis, M. 1998, *ApJ*, 500, 525
- Shu, F. H., Adams, F. C., & Lizano, S. 1987, *ARA&A*, 25, 23
- Silva, G. M. D., Freeman, K. C., Bland-Hawthorn, J., et al. 2015, *MNRAS*, 449, 2604
- Simonian, G. V. A., Pinsonneault, M. H., & Terndrup, D. M. 2019, *ApJ*, 871, 174
- Skumanich, A. 1972, *ApJ*, 171, 565
- Soderblom, D. R. 2010, *ARA&A*, 48, 581
- Soderblom, D. R., Jones, B. F., Balachandran, S., et al. 1993, *AJ*, 106, 1059
- Spada, F., & Lanzafame, A. C. 2020, *A&A*, 636, A76
- Spitzer, Jr., L. 1958, *ApJ*, 127, 17
- Stassun, K. G., Oelkers, R. J., Paegert, M., et al. 2019, *AJ*, 158, 138
- Stauffer, J. R., Jones, B. F., Backman, D., et al. 2003, *AJ*, 126, 833
- Stellingwerf, R. F. 1978, *ApJ*, 224, 953
- Stellingwerf, R. F. 2011, , 47, conference Name: RR Lyrae Stars, Metal-Poor Stars, and the Galaxy Place: eprint: arXiv:1108.4984
- Sullivan, P. W., Winn, J. N., Berta-Thompson, Z. K., et al. 2015, *ApJ*, 809, 77
- Tang, S.-Y., Pang, X., Yuan, Z., et al. 2019, *ApJ*, 877, 12
- Tian, H.-J. 2020, *ApJ*, 904, 196, publisher: American Astronomical Society
- Tokovinin, A. 2018, *PASP*, 130, 035002
- Tokovinin, A., Fischer, D. A., Bonati, M., et al. 2013, *PASP*, 125, 1336
- Wallace, J. J. 2018, *Res. Notes AAS*, 2, 213
- Walt, S. v. d., Colbert, S. C., & Varoquaux, G. 2011, *Computing in Science & Engineering*, 13, 22
- Weber, E. J., & Davis, Jr., L. 1967, *ApJ*, 148, 217
- Wright, N. J., & Mamajek, E. E. 2018, *MNRAS*, 476, 381
- Zari, E., Hashemi, H., Brown, A. G. A., Jardine, K., & de Zeeuw, P. T. 2018, *Astronomy and Astrophysics*, 620, A172
- Zucker, C., Battersby, C., & Goodman, A. 2018, *ApJ*, 864, 153
- Zuckerman, B., & Song, I. 2004, *ARA&A*, 42, 685

APPENDIX

A. CLUSTERING METHODS AND OUTCOMES

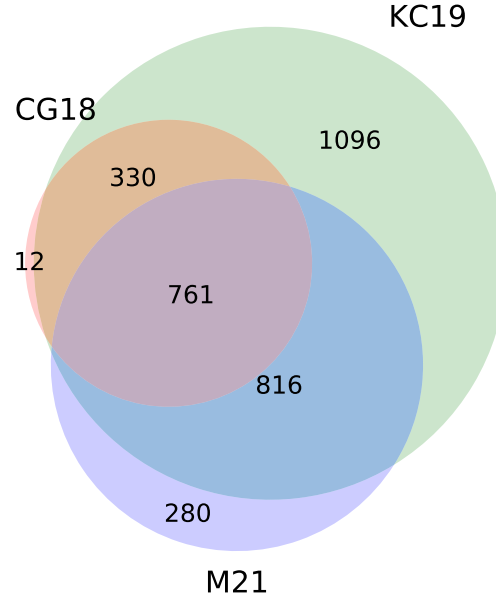


Figure 8. Different clustering techniques yield different outcomes. 3,298 unique candidate cluster members found using three different techniques are considered in this study. CG18: Cantat-Gaudin et al. (2018), KC19: Kounkel & Covey (2019), M21: Meingast et al. (2021).

Figure 8 is a Venn diagram showing the overlap between the three membership catalogs concatenated in this study. 99% of the CG18 sample overlaps with KC19, M21, or both. By comparison, 36% of the KC19 sample, and 15% of the M21 sample are non-overlapping. The data—Gaia DR2—used by all the studies was the same. What are the differences in methodology that produce these different outcomes?

CG18 applied a procedure that yielded what we call “the core”. Their procedure was to first query a Gaia DR2 cone around the previously reported RA and dec of the cluster, and within ± 0.5 mas of its previously reported distance. The outer radius of their cone was either r_2 from MWSC (CITE Kharchenko 2013), or twice the “cluster radius” listed by DAML/Dias (CITE). No proper motion cut was applied. They then applied an unsupervised classification scheme called UPMASK to $G < 18$ mag stars within this cone (CITE). The steps of UPMASK are first to perform a k-means clustering in the “astrometric space” ($\mu_{\alpha'}, \mu_{\delta}, \pi$). Then, a “veto” step is applied to assess whether the groups of stars output from the k-means clustering are or are not more concentrated than a random distribution. This is implemented by “comparing the total branch length of the minimum spanning tree connecting the stars with the expected branch length for a random uniform distribution covering the investigated field of view”. To turn this yes/no flag to a membership probability, Cantat-Gaudin et al. (2018) then redraw new values of ($\mu_{\alpha'}, \mu_{\delta}, \pi$) for each source based on the listed value, uncertainty, and covariance. After a certain number of redrawings, the final probability is the frequency with which a given star passes the veto”. In the case of NGC 2516, this yielded a reported “ r_{50} ” within which half of the cluster members were found to be within 0.496° . When we selected candidate NGC 2516 members from the results of CG18, we opted to include all candidate members with reported membership probability exceeding 10%. While this seems *a priori* low, our results (SECTION XXX) show that this “membership probability” severely underestimates the purity of the CG18 sample for NGC 2516. Their false positive rate across the sample is more like 1-5%.

KC19 applied a different unsupervised clustering method to the 5-dimensional Gaia DR2 data (omitting radial velocities, due to their sparsity). Their selection function (see their Section 2) yielded $\approx 2 \times 10^7$ stars, mostly within ≈ 1 kpc and typically with $G < 18$ mag. Their clustering algorithm, which was run on this entire stellar sample, was the “hierarchical density-based spatial clustering of applications with noise” (HDBSCAN, CITE McInnes17). The classical DBSCAN algorithm “identifies clusters as overdensities in a multi-dimensional space in which the number of sources exceeds the required minimum number of points within a neighborhood of a particular linking length ϵ . HDBSCAN does not depend on ϵ ; instead it condenses the minimum spanning tree by pruning off the nodes that do not meet the minimum number of sources in a cluster and reanalyzing the nodes that do. Depending on the chosen algorithm, it would then either find the most persistent structure (through the excess of mass

method), or return clusters as the leaves of the tree (which results in somewhat more homogeneous clusters). In both cases it is more effective at finding structures of varying densities in a given data set than DBSCAN.” “The two main parameters that control HDBSCAN are the number of sources in a cluster and the number of samples. The former is the parameter that rejects groupings that are too small; the latter sets the threshold of how conservative the algorithm is in its considerations of the background noise (even if the resulting noisy groupings do meet the minimum cluster size). By default, the sample size is set to the same value as the cluster size, but it is possible to adjust them separately.” Regarding membership probabilities, KC19 did not report continuous membership probabilities, instead opting for the binary “member” or “not”.

M21 did the same as KC19, but required A) the tangential velocity dispersions to be smaller, and B) deconvolved the distances.
FIXME **FIXME** **FIXME** **FIXME** **FIXME** **FIXME** **FIXME**

Meingast et al. (2021) reported a Finally, 1577 of the 1860 Meingast et al. (2021) sources (85%) were included in the Kounkel & Covey (2019) sample.

B. DETRENDING DETAILS

In “detrending” for our general variability search, our goal was to preserve astrophysical variability, while removing systematic variability. One particular concern for the TESS light curves is systematic variability at the timescale of the 14-day satellite orbit, mostly induced by scattered light from the Earth and Moon.

We therefore turned to the principal components (i.e., the eigenvectors) calculated following the procedure described by Bouma et al. (2019). In brief, these vectors are computed using a set of “trend stars” selected from across each CCD according to ad-hoc heuristics that (hopefully) lead them to be dominated by *systematic* variability (Sec 3.7.2).

The principal component vectors, also referred to as the eigenvectors, are rank-ordered by the degree of variance that they predict in the training set (of “trend stars”).

We then posit that any given target star’s light curve is described as a linear combination of the eigenvectors. Optionally, we also considered the inclusion of additional systematic vectors that could affect the light curve, such as the CCD temperature, the flux level measured in the background annulus, and the centroid positions of the stars on the CCDs. These can be treated as additional “features” in the linear model.

To determine the coefficients of the linear model after the full set of eigenvectors (plus optionally “sytematic” vectors) had been assembled, we explored two possible methods: ordinary least squares, and ridge regression. Ridge regression is the same as ordinary least squares, except it includes an L2 norm with a regularization coefficient. The regularization coefficient that best applied for any given target light curve was solved for using a cross-validation grid search, using `sklearn.linear_modelRidgeCV` (CITE).

Each target light curve was mean-subtracted and normalized by its standard deviation, as were the eigenvectors. The linear problem was then solved numerically, and the light curve was reconstructed by re-adding the original mean, and re-multiplying by the standard deviation to ensure that the variance of the light curve did not change.

We found that the choice of using ordinary least squares versus ridge regression did not seem to significantly affect the resulting light curves. In other words, the inclusion (or lack thereof) of a regularization term did not strongly alter the best-fitting coefficients. In the spirit of “KISS”, we opted to use ordinary least squares.

A few other choices seemed to be more important:

- *To smooth, or to not smooth the eigenvectors.* Ideally, the eigenvectors should be smooth in time. They should not contain residuals from e.g., eclipsing binaries that snuck their way into the template set, and they should also not be intrinsically noisier than the target star. If either of these is the case (and we found that it sometimes was), it can induce extra variability into the PCA “detrended” light curves. To address this problem, we opted to smooth the eigenvectors using a time-windowed filter (with a “biweight” weight scheme, implemented in `wotan` by Hippke et al. (2019); window length 1 day, `cval` 6). One issue with this is that systematic sharp features (captured e.g., in “spike vectors”) no longer are captured, so they end up in the “PCA detrended” light curves. They can then be filtered out (e.g., using rolling outlier rejection), and we prefer this approach to having systematic features being *injected* by the PCA detrending.
- *How many eigenvectors to use.* A larger number always leads to greater whitening. In Bouma et al. (2019), we performed a Factor Analysis cross-validation to determine the number of eigenvectors to use. The typical number adopted based on this analysis was 10–15. While this approach should in theory prevent over-fitting, in our experience, for stellar rotation it still often lead to distorts the signals, especially for rotation signals with small amplitudes and periodicities of $\gtrsim 3$ days. (Shorter signals typically are not distorted, since the eigenvectors do not contain the high-frequency content that leads to the distortions). For the present analysis, we therefore impose the maximum number of eigenvectors to be 5.
- *Which supplementary systematics vectors to use.* We considered using the BGV, CCDTEMP, XIC, YIC, and BGV vectors, packaged with the CDIPS light curves. We found that the background value measured in an annulus centered on the aperture, BGV, tended to produce the best independent information from the PCA eigenvectors, and so we adopted it as

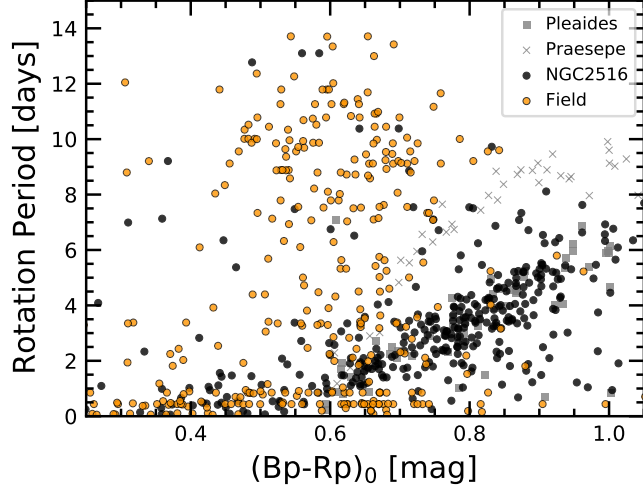


Figure 9. Rotation in NGC 2516 compared to the field. Stars with Gaia $Rp < 13$ mag in the cluster and field samples were considered. (Fainter stars in the field sample were not studied as part of the broader CDIPS project). The field stars show a different rotation period distribution than the kinematically selected NGC 2516 members.

our only “supplementary” trend vector. We opted to not smooth it (in hopes that it would provide direct complement to the smoothed PCA vectors; 1 sharp vector containing literally the background information, plus 5 smooth vectors).

For every “target star”, we then decorrelated the raw (image-subtracted and background-subtracted) light curve using a linear model with ordinary least squares.

C. COMPARISON STAR ROTATION PERIODS

To provide a basis for comparison, we also opted to search the “calibration” light curves ($Rp < 13$) that were created as a part of the CDIPS project. Over the southern sky (Sectors 1-13 of TESS), this corresponded to a sample of 9,619,784 stars. Cross-matching these against the 13,843 randomly drawn stars in the neighborhood of NGC 2516 yielded 1,987 unique stars, with a cumulative total of 9,790 TESS sectors observed. The magnitude cut of $Rp < 13$ at the distances of the neighborhood sample corresponds to an extinction-corrected color cutoff of $(Bp - Rp)_0 \approx 0.80$, or spectral types of $\approx G1V$. This reaches sufficiently far down the main-sequence to enable a comparison to the cluster star sample.

We performed the same light curve stitching and period-search procedure on the field comparison stars. Imposing the same requirements for crowding resulted in 820 stars for which rotation periods could have been detected. Imposing the same Lomb Scargle power cutoff, and period upper limit, yielded 365 period detections (44.5%). Within the same brightness cutoff, 374 of 705 cluster stars yielded period detections (53.1%). Though the detection fractions are frankly not very different (likely because of the brightness cutoff), the period vs color distributions are quite different (Figure 9).

D. PROJECTION EFFECTS FOR 2D VELOCITIES

Figure 10 shows why the correct approach for comparing any star’s proper motions against the cluster’s mean depends on the position of the star being considered.

E. DIFFERENTIAL REDDENING

Figure 11.

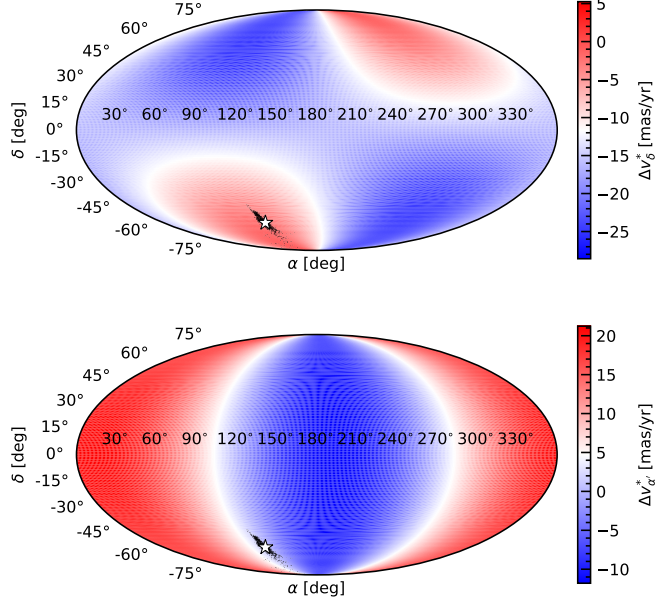


Figure 10. Projection effects for co-moving populations across the sky. The map is colored by the velocity difference a star co-moving with NGC 2516 would exhibit across the equatorial sphere. Actual positions of candidate NGC 2516 members are shown with points; the star denotes the cluster center.

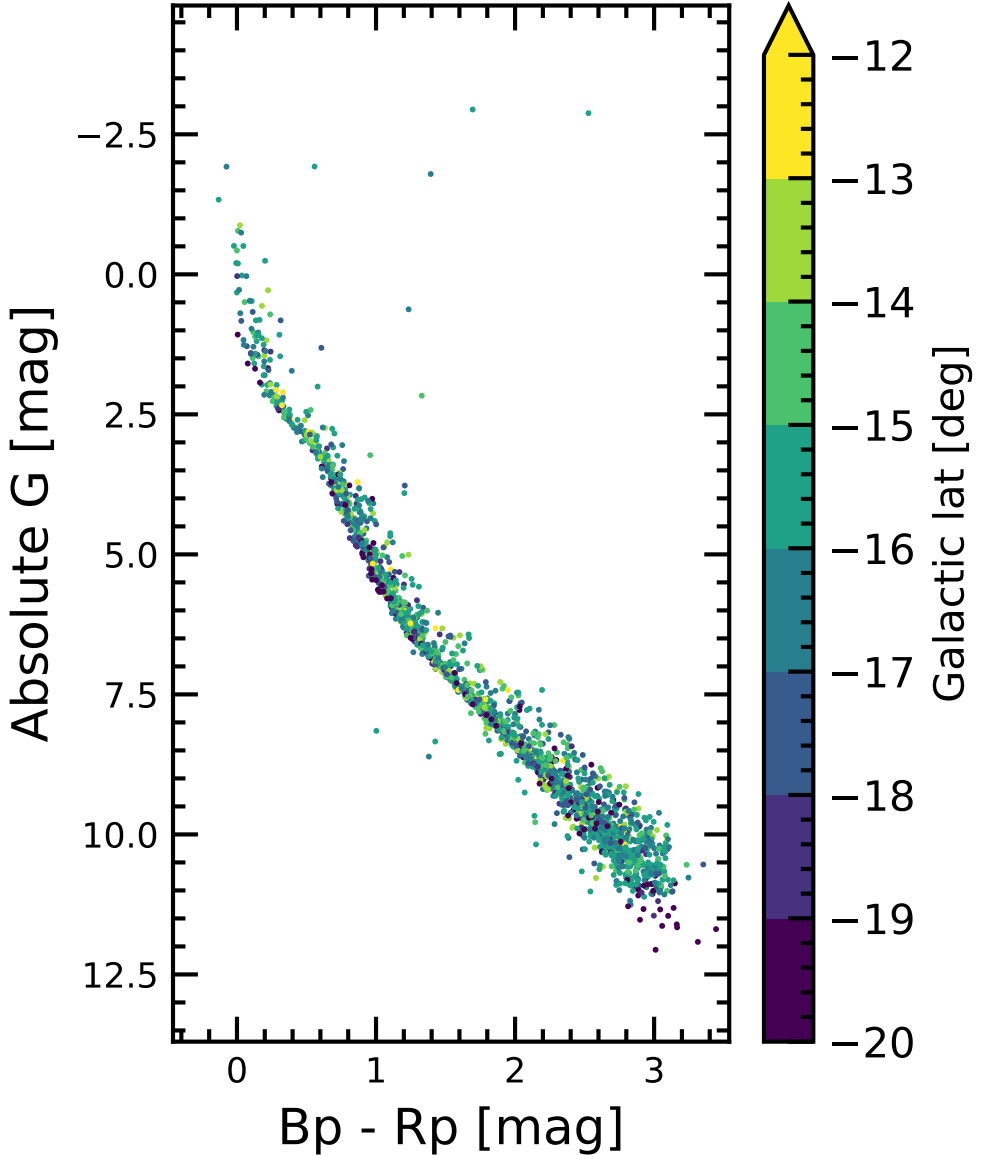


Figure 11. HR diagram of NGC 2516, using Gaia EDR3 photometry. *Bottom:* Reported members of the halo, as a function of galactic latitude. Can the additional scatter in the halo be understood through differential reddening? **Maybe.**